Inclusive $D^{*\pm}$ meson cross sections and $D^{*\pm}$-jet correlations in photoproduction at HERA

H1 Collaboration

A. Aktas[9], V. Andreev[25], T. Anthonis[3], B. Antunovic[26], S. Aplin[9], A. Asmone[33], A. Astvatsatourov[3],
A. Babaev[24,a], S. Backovic[30], A. Baghdasaryan[37], P. Baranov[25], E. Barrelet[29], W. Bartel[9], S. Baudrand[27],
S. Baumgartner[39], M. Beckingham[9], O. Behnke[12,b], O. Behrendt[6], A. Belousov[25], N. Berger[39], J.C. Bizot[27],
M.-O. Boenig[6], V. Boudry[28], J. Bracinik[26], G. Brandt[12], V. Brisson[27], D. Bruncko[15], F.W. Büsser[10],
A. Bunyatyan[11,37], G. Buschhorn[26], L. Bystritskaya[24], A.J. Campbell[9], S. Caron[1,48], F. Cassol-Brunner[21],
K. Cerny[32], V. Cerny[15,46], V. Chekelian[26], J.G. Contreras[22], J.A. Coughlan[4], B.E. Cox[20], G. Cozzika[8], J. Cvach[31],
J.B. Dainton[17], W.D. Dau[14], K. Daum[36,42], Y. de Boer[24], B. Delcourt[27], M. Del Degan[39], A. De Roeck[9,44],
E.A. De Wolf[3], C. Diaconu[21], V. Dodonov[11], A. Dubak[30,45], G. Eckerlin[9], S. Egli[35], R. Eichler[35],
F. Eisele[12], A. Eliseev[25], E. Elsen[9], S. Essenov[24], A. Falkewicz[5], P.J.W. Faulkner[2], L. Favart[3], A. Fedotov[24],
R. Felst[9], J. Feltesse[8,47], J. Ferencei[15], L. Finke[10], M. Fleischer[9], G. Flucke[10], A. Fomenko[25], G. Franke[9],
T. Frisson[28], E. Gabathuler[17], E. Garutti[9], J. Gayler[9], C. Gerlich[12], S. Ghazaryan[37], S. Ginzburgskaya[24],
A. Glazov[9], I. Glushkov[38], L. Goerlich[5], M. Goettlich[9], N. Gogitidze[25], S. Gorbounov[38], C. Grab[39], T. Greenshaw[17],
M. Gregori[18], B.R. Grell[9], G. Grindhammer[26], C. Gwilliam[20], S. Habib[10], D. Haidt[9], M. Hansson[19],
G. Heinzelmann[10], R.C.W. Henderson[16], H. Henschel[38], G. Herrera[23], M. Hildebrandt[35], K.H. Hiller[38],
D. Hoffmann[21], R. Horisberger[35], A. Hovhannisyan[37], T. Hreus[3,43], S. Hussain[18], M. Ibbotson[20], M. Ismail[20],
M. Jacquet[27], X. Janssen[3], V. Jemanov[10], L. Jönsson[19], D.P. Johnson[3], A.W. Jung[13], H. Jung[19,9], M. Kapichine[7],
J. Katzy[9], I.R. Kenyon[2], C. Kiesling[26], M. Klein[38], C. Kleinwort[9], T. Klimkovich[9], T. Kluge[9], G. Knies[9],
A. Knutsson[19], V. Korbel[9], P. Kostka[38], K. Krastev[9], J. Kretzschmar[38], A. Kropivnitskaya[24], K. Krüger[13],
M.P.J. Landon[18], W. Lange[38], G. Laštovička-Medin[30], P. Laycock[17], A. Lebedev[25], G. Leibenguth[39],
V. Lendermann[13], S. Levonian[9], L. Lindfeld[40], K. Lipka[38], A. Liptaj[26], B. List[10], J. List[10], E. Lobodzinska[38,5],
N. Loktionova[25], R. Lopez-Fernandez[23], V. Lubimov[24], A.-I. Lucaci-Timoce[9], H. Lueders[10], T. Lux[10], L. Lytkin[11],
A. Makankine[7], N. Malden[20], E. Malinovski[25], P. Marage[3], R. Marshall[20], L. Marti[9], M. Martisikova[9],
H.-U. Martyn[1], S.J. Maxfield[17], A. Mehta[17], K. Meier[13], A.B. Meyer[9], H. Meyer[36], J. Meyer[9], V. Michels[9],
S. Mikocki[5], I. Milcewicz-Mika[5], D. Milstead[17], D. Mladenov[34], A. Mohamed[17], F. Moreau[28], A. Morozov[7],
J.V. Morris[4], M.U. Mozer[12], K. Müller[40], P. Murín[15,43], K. Nankov[34], B. Naroska[10], Th. Naumann[38],
P.R. Newman[2], C. Niebuhr[9], A. Nikiforov[26], G. Nowak[5], K. Nowak[40], M. Nozicka[32], R. Oganezov[37], B. Olivier[26],
J.E. Olsson[9], S. Osman[19], D. Ozerov[24], V. Palichik[7], I. Panagoulias[9,41], T. Papadopoulou[9,41], C. Pascaud[27],
G.D. Patel[17], H. Peng[9], E. Perez[8], D. Perez-Astudillo[22], A. Perieanu[9], A. Petrukhin[24], D. Pitzl[9], R. Plačakytė[26],
B. Portheault[27], B. Povh[11], P. Prideaux[17], A.J. Rahmat[17], N. Raicevic[30], P. Reimer[31], A. Rimmer[17], C. Risler[9],
E. Rizvi[18], P. Robmann[40], B. Roland[3], R. Roosen[3], A. Rostovtsev[24], Z. Rurikova[26], S. Rusakov[25], F. Salvaire[10],
D.P.C. Sankey[4], M. Sauter[39], E. Sauvan[21], S. Schmidt[9], S. Schmitt[9], C. Schmitz[40], L. Schoeffel[8], A. Schöning[39],
H.-C. Schultz-Coulon[13], F. Sefkow[9], R.N. Shaw-West[2], I. Sheviakov[25], L.N. Shtarkov[25], T. Sloan[16], P. Smirnov[25],
Y. Soloviev[25], D. South[9], V. Spaskov[7], A. Specka[28], M. Steder[9], B. Stella[33], J. Stiewe[13], A. Stoilov[34],
U. Straumann[40], D. Sunar[3], V. Tchoulakov[7], G. Thompson[18], P.D. Thompson[2], T. Toll[9], F. Tomasz[15],
D. Traynor[18], T.N. Trinh[21], P. Truöl[40], I. Tsakov[34], G. Tsipolitis[9,41], I. Tsurin[9], J. Turnau[5], E. Tzamariudaki[26],
K. Urban[13], M. Urban[40], A. Usik[25], D. Utkin[24], A. Valkárová[32], C. Vallée[21], P. Van Mechelen[3], A. Vargas Trevino[6],
Y. Vazdik[25], C. Veelken[17], S. Vinokurova[9], V. Volchinski[37], K. Wacker[6], G. Weber[10], R. Weber[39], D. Wegener[6],
C. Werner[12], M. Wessels[9], B. Wessling[9], Ch. Wissing[6], R. Wolf[12], E. Wünsch[9], S. Xella[40], W. Yan[9], V. Yeganov[37],
J. Žáček[32], J. Zálešák[31], Z. Zhang[27], A. Zhelezov[24], A. Zhokin[24], Y.C. Zhu[9], J. Zimmermann[26], T. Zimmermann[39],
H. Zohrabyan[37], F. Zomer[27]

[1] I. Physikalisches Institut der RWTH, Aachen, Germany[c]
[2] School of Physics and Astronomy, University of Birmingham, Birmingham, UK[d]
[3] Inter-University Institute for High Energies ULB-VUB, Brussels; Universiteit Antwerpen, Antwerpen, Belgium[e]
[4] Rutherford Appleton Laboratory, Chilton, Didcot, UK[d]
[5] Institute for Nuclear Physics, Cracow, Poland[f]
[6] Institut für Physik, Universität Dortmund, Dortmund, Germany[c]
[7] Joint Institute for Nuclear Research, Dubna, Russia
[8] CEA, DSM/DAPNIA, CE-Saclay, Gif-sur-Yvette, France

[9] DESY, Hamburg, Germany
[10] Institut für Experimentalphysik, Universität Hamburg, Hamburg, Germany[c]
[11] Max-Planck-Institut für Kernphysik, Heidelberg, Germany
[12] Physikalisches Institut, Universität Heidelberg, Heidelberg, Germany[c]
[13] Kirchhoff-Institut für Physik, Universität Heidelberg, Heidelberg, Germany[c]
[14] Institut für Experimentelle und Angewandte Physik, Universität Kiel, Kiel, Germany
[15] Institute of Experimental Physics, Slovak Academy of Sciences, Košice, Slovak Republic[g]
[16] Department of Physics, University of Lancaster, Lancaster, UK[d]
[17] Department of Physics, University of Liverpool, Liverpool, UK[d]
[18] Queen Mary and Westfield College, London, UK[d]
[19] Physics Department, University of Lund, Lund, Sweden[h]
[20] Physics Department, University of Manchester, Manchester, UK[d]
[21] CPPM, CNRS/IN2P3 - Univ. Mediterranee, Marseille, France
[22] Departamento de Fisica Aplicada, CINVESTAV, Mérida, Yucatán, México[i]
[23] Departamento de Fisica, CINVESTAV, México[i]
[24] Institute for Theoretical and Experimental Physics, Moscow, Russia[j]
[25] Lebedev Physical Institute, Moscow, Russia[k]
[26] Max-Planck-Institut für Physik, München, Germany
[27] LAL, Université de Paris-Sud 11, IN2P3-CNRS, Orsay, France
[28] LLR, Ecole Polytechnique, IN2P3-CNRS, Palaiseau, France
[29] LPNHE, Universités Paris VI and VII, IN2P3-CNRS, Paris, France
[30] Faculty of Science, University of Montenegro, Podgorica, Serbia and Montenegro[j]
[31] Institute of Physics, Academy of Sciences of the Czech Republic, Praha, Czech Republic[l]
[32] Faculty of Mathematics and Physics, Charles University, Praha, Czech Republic[l]
[33] Dipartimento di Fisica Università di Roma Tre and INFN Roma 3, Roma, Italy
[34] Institute for Nuclear Research and Nuclear Energy, Sofia, Bulgaria[k]
[35] Paul Scherrer Institut, Villigen, Switzerland
[36] Fachbereich C, Universität Wuppertal, Wuppertal, Germany
[37] Yerevan Physics Institute, Yerevan, Armenia
[38] DESY, Zeuthen, Germany
[39] Institut für Teilchenphysik, ETH, Zürich, Switzerland[m]
[40] Physik-Institut der Universität Zürich, Zürich, Switzerland[m]
[41] Also at Physics Department, National Technical University, Zografou Campus, 15773 Athens, Greece[n]
[42] Also at Rechenzentrum, Universität Wuppertal, Wuppertal, Germany
[43] Also at University of P.J. Šafárik, Košice, Slovak Republic
[44] Also at CERN, Geneva, Switzerland
[45] Also at Max-Planck-Institut für Physik, München, Germany
[46] Also at Comenius University, Bratislava, Slovak Republic
[47] Also at DESY and University Hamburg, Helmholtz Humboldt Research Award
[48] Now at Physikalisches Institut, Universität Freiburg, Freiburg i. Br., Germany

Abstract. Differential photoproduction cross sections are measured for events containing $D^{*\pm}$ mesons. The data were taken with the H1 detector at the *ep* collider HERA and correspond to an integrated luminosity of $51.1\,\mathrm{pb}^{-1}$. The kinematic region covers small photon virtualities $Q^2 < 0.01\,\mathrm{GeV}^2$ and photon–proton centre-of-mass energies of $171 < W_{\gamma p} < 256\,\mathrm{GeV}$. The details of the heavy quark production process are further investigated in events with one or two jets in addition to the $D^{*\pm}$ meson. Differential cross sections for $D^* + jet$ production are determined and the correlations between the $D^{*\pm}$ meson and the jet(s) are studied. The results are compared with perturbative QCD predictions applying collinear- or k_t-factorisation.

[a] Deceased

[b] e-mail: obehnke@mail.desy.de

[c] Supported by the Bundesministerium für Bildung und Forschung, FRG, under contract numbers 05 H1 1GUA /1, 05 H1 1PAA /1, 05 H1 1PAB /9, 05 H1 1PEA /6, 05 H1 1VHA /7 and 05 H1 1VHB /5

[d] Supported by the UK Particle Physics and Astronomy Research Council, and formerly by the UK Science and Engineering Research Council

[e] Supported by FNRS-FWO-Vlaanderen, IISN-IIKW and IWT and by Interuniversity Attraction Poles Programme, Belgian Science Policy

[f] Partially Supported by the Polish State Committee for Scientific Research, SPUB/DESY/P003/DZ 118/2003/2005

[g] Supported by VEGA SR grant no. 2/4067/ 24

[h] Supported by the Swedish Natural Science Research Council

[i] Supported by CONACYT, México, grant 400073-F

a) Direct γ b) Real Gluon Emission   c) Excitation   d) Hadron - like
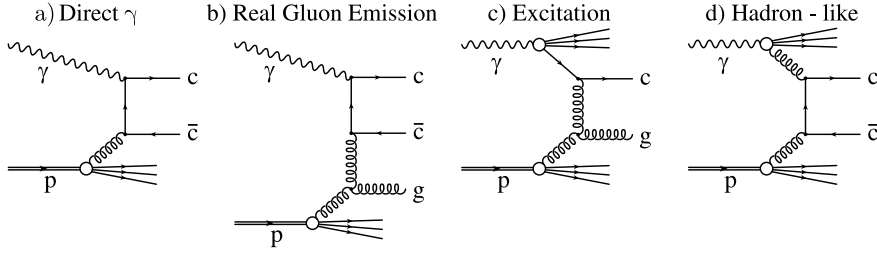
Fig. 1. Diagrams for charm photoproduction: direct photon processes (**a**) and (**b**), and resolved photon processes with **c** charm excitation and **d** the hadronic manifestation of the real photon

1 Introduction

Charm photoproduction in ep collisions at HERA proceeds predominantly via photon-gluon fusion as shown in Fig. 1, where the quasi real photon (virtuality $Q^2 \simeq 0\,\mathrm{GeV}^2$) is emitted from the beam lepton. The charm quark mass provides a hard scale which allows perturbative QCD (pQCD) to be applied over the full phase space. Therefore, charm photoproduction is particularly well suited to test perturbative calculations and the underlying theoretical approaches.

Previous measurements have focused on inclusive $D^{*\pm}$ meson production [1, 2], $D^{*\pm}$ meson with associated dijet production [2–4] and heavy quark pair production using events with a $D^{*\pm}$ meson and a muon [5]. Here $D^{*\pm}$ photoproduction is considered, using a data sample five times larger than in the previous H1 analysis [1]. Single and double differential cross sections for inclusive $D^{*\pm}$ production are presented and compared with theoretical calculations using collinear-factorisation [6–10] or k_t-factorisation [11–14]. Details of the heavy quark production process are investigated further by studying events either with an additional jet not containing the D^* meson ("$D^* + other\ jet$") or with two jets ("$D^*\ tagged\ dijet$"). The jets are measured down to a transverse momentum of $p_t(\text{jet}) = 3\,\mathrm{GeV}$, which extends the region explored in [2–4] to significantly smaller values. Whereas the D^* always originates from a charm or anticharm quark produced in the hard subprocess, the non-D^*-tagged jet can result from either the other heavy quark (Fig. 1a, b, d) or a light parton (e.g. a gluon, Fig. 1b and c). Measurements of correlations between the D^* and the jet are performed which are sensitive to higher order effects and to the longitudinal and transverse momenta of the partons entering the hard scattering process.

The paper is organised as follows. In Sect. 2 a brief description of the H1 detector is given, followed by the details of the event selection and the reconstruction of the D^* mesons. In Sect. 4 the theoretical calculations are described. In Sect. 5 the determination of the cross sections and the systematic uncertainties are presented and

the measured cross sections are compared with theoretical calculations.

2 Detector description

The H1 detector is described in detail in [15, 16] and only the components most relevant for this analysis are briefly mentioned here. The origin of the H1 coordinate system is the nominal ep interaction point, the direction of the proton beam defining the positive z-axis (forward region). The transverse momenta are measured in the xy plane.

Charged particles are measured in the central tracking detector (CTD) which covers the range in pseudorapidity[1] $1.74 > \eta > -1.74$. The CTD comprises two large cylindrical central jet chambers (CJCs) arranged concentrically around the beam-line within a solenoidal magnetic field of 1.15 T. Two additional drift chambers improve the z-coordinate reconstruction. The track resolution is further improved using hit information from the central silicon track detector (CST) [17]. The CTD also provides trigger information which is based on measurements in the r-ϕ plane of the CJCs and the z-position of the interaction vertex obtained from a double layer of multiwire proportional chambers. The specific ionisation energy loss of charged particles, $\mathrm{d}E/\mathrm{d}x$, is derived from the mean of the inverse square-root of the charge collected by all CJC sense wires with a signal above a certain threshold. The average resolution for minimum ionising particles is $\sigma(\mathrm{d}E/\mathrm{d}x)/(\mathrm{d}E/\mathrm{d}x) \simeq 8\%$ [18].

The track detectors are surrounded in the forward and central directions by a fine grained liquid argon calorimeter (LAr, $3.4 > \eta > -1.5$) and in the backward region by a lead-scintillating fibre calorimeter (SpaCal, $-1.4 > \eta > -4.0$) [19] both of which contain electromagnetic and hadronic sections. For the present analysis the hadronic final state (HFS) is reconstructed from combined objects, built from calorimeter clusters and tracks, using an algorithm which ensures that no double counting of energy occurs. Compared to the case of clusters alone the use of combined objects improves the reconstruction of low momentum particles.

A crystal Čerenkov calorimeter (electron tagger) located close to the beam pipe at $z = -33.4$ m detects beam leptons scattered through a very small angle $(\pi - \theta_{e'}) <$

---

[1] The pseudo-rapidity η corresponding to a polar angle θ (measured with respect to the positive z-axis) is given by $\eta = -\ln \tan(\theta/2)$.

Table 1. D^* selection cuts and definition of the *"visible"* kinematic regions for which the *inclusive D^**, the *$D^* + other$ jet* and the *D^* tagged dijet* cross sections are measured

Selection of $D^{*+} \to D^0 \pi_s^+ \to K^- \pi^+ \pi_s^+$	$p_t(K, \pi) > 0.3$ GeV $p_t(\pi_s) > 0.12$ GeV $20^\circ < \theta(K, \pi, \pi_s) < 160^\circ$ $dE/dx(K, \pi, \pi_s)$ consistent with particle hypothesis $\|m(K\pi) - m_{D^0}\| \leq \begin{cases} 80 \text{ MeV for } p_t(D^*) < 6.0 \text{ GeV} \\ 100 \text{ MeV for } 6.0 \leq p_t(D^*) < 8.5 \text{ GeV} \\ 140 \text{ MeV for } p_t(D^*) \geq 8.5 \text{ GeV} \end{cases}$ $\Delta m = m(K\pi\pi_s) - m(K\pi) < 167.5$ MeV $p_t(K) + p_t(\pi) > 2.2$ GeV $\frac{p_t(D^*)}{\sum_{\text{HFS}}^{\theta > 10^\circ} E_{t,i}} > 0.10$
Visible kinematic region	*inclusive D^**
	$p_t(D^*) \geq 2.0$ GeV $\|\eta(D^*)\| < 1.5$ $Q^2 < 0.01$ GeV^2 $0.29 < y < 0.65$

$D^* + other$ jet	*D^* tagged dijet*
$\|\eta(\text{jet})\| < 1.5$	$\|\eta(\text{jet})\| < 1.5$
$p_t(\text{jet}) \geq 3$ GeV	$p_t(\text{jet}_1) \geq 4$ GeV
$D^* \notin \text{jet}$	$p_t(\text{jet}_2) \geq 3$ GeV

5 mrad and is used to trigger photoproduction events. The ep luminosity is determined from the QED bremsstrahlung $(ep \to ep\gamma)$ event rate by detecting the radiated photon in another Čerenkov calorimeter located at $z = -103$ m (photon detector).

3 Event selection and reconstruction

The data were recorded in e^+p scattering at HERA in 1999 and 2000 and correspond to an integrated luminosity of $\mathcal{L} = 51.1$ pb^{-1}. The energy of the positrons was $E_e = 27.6$ GeV and that of the protons $E_p = 920$ GeV.

The events were triggered by requiring signals from the central drift chambers and the multi-wire proportional chambers in coincidence with a signal in the electron tagger. In addition, an on-line software filter selected events with candidates for charmed hadron decays by calculating invariant masses of track combinations.

The analysis of photoproduction events is restricted to $0.29 < y < 0.65$, where the inelasticity $y = 1 - E_{e'}/E_e$ is calculated from the reconstructed positron energy $E_{e'}$ in the tagger. In this y-range the average tagger acceptance is almost 40%. This range corresponds to a photon–proton centre-of-mass energy $171 \lesssim W_{\gamma p} \lesssim 256$ GeV. For the small scattering angles considered the photon virtuality Q^2 is below 0.01 GeV^2.

3.1 D^* selection and fit

The $D^{*\pm}$ meson is detected via the decay channel[2] $D^{*+} \to D^0 \pi_s^+ \to K^- \pi^+ \pi_s^+$, which has a branching ratio $\mathcal{BR}(D^* \to$

---

[2] Charge conjugate states are implicitly implied.

$K\pi\pi_s) = (2.57 \pm 0.06)\%$ [20]. Here π_s refers to the low momentum pion from the D^* decay. In each event, tracks with opposite charges, fitted to the event vertex, are combined in pairs and both invariant masses $m(K^\pm\pi^\mp)$ are calculated where one track is assigned the kaon mass and the other the pion mass. If the result is consistent with the nominal D^0 mass [20], any remaining track with a charge opposite to that of the kaon candidate is assigned the pion mass and combined with the D^0 candidate to form a D^* candidate. The measured specific energy loss per path length dE/dx of each track has to be consistent with the respective particle hypothesis [21]. Using dE/dx improves the signal-to-background ratio for D^* candidates by about 20%.

The D^* candidate is accepted if it fulfils the selection cuts listed in Table 1. The restrictions in the transverse momentum $p_t(D^*)$ and in the pseudorapidity $\eta(D^*)$ ensure good detector acceptance. To reduce the combinatorial background, cuts are applied to the scalar sum of $p_t(K)$ and $p_t(\pi)$ and to the fraction of the transverse momentum carried by the D^* with respect to the scalar sum of transverse energies of the full hadronic final state, excluding the forward region $(\theta < 10^\circ)$.

In Fig. 2a the distribution of the mass difference $\Delta m = m(K\pi\pi_s) - m(K\pi)$ of the final D^* candidates is shown. A clear peak is observed around the nominal value of $\Delta m = (145.421 \pm 0.010)$ MeV [20]. The number of reconstructed D^* mesons $N(D^*)$ is extracted from a likelihood fit to the Δm-distribution with a function which is a superposition of a Gaussian for the signal and a phase space threshold function with a quadratic correction term, $F^b(\Delta m) = u_n(\Delta m - m_\pi)^{u_e} \cdot (1 - u_s(\Delta m)^2)$, for the background. The fit yields a signal of 1166 ± 82 D^* mesons. Separate fits are performed in each bin of the cross section measurement, in
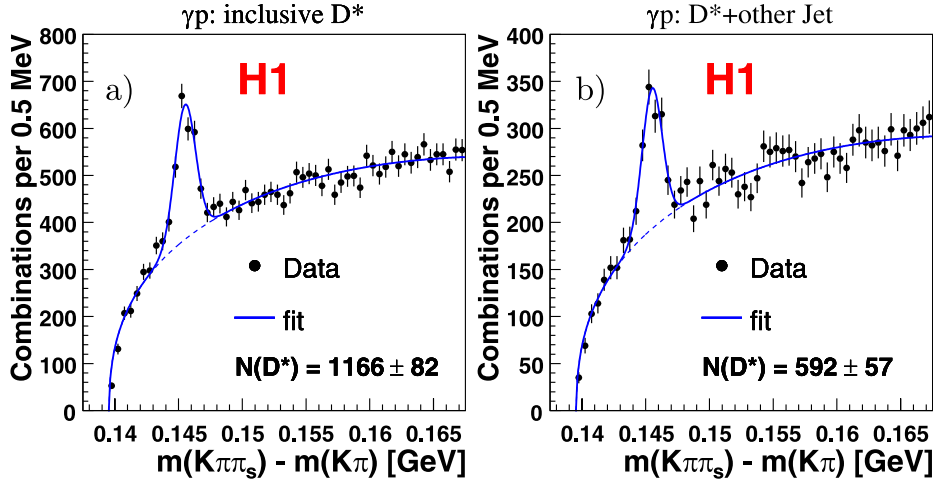
Fig. 2. D^* signal in the distribution of the mass difference $\Delta m = m(K\pi\pi_s) - m(K\pi)$ of the *inclusive* D^* (**a**) and the $D^* + other\ jet$ (**b**) selection. The *solid lines* represent the fits to determine the number of D^* mesons in the signal and the *dashed lines* indicate the resulting background parametrisations

Table 2. Jet resolutions (RMS) in p_t and η as obtained from the simulations for different ranges of p_t from hadron to detector level (middle column) and from parton to hadron level (right column)

Jet Resolutions (RMS)		
range	$(p_{t\ det} - p_{t\ had})/p_{t\ had}$	$(p_{t\ had} - p_{t\ part})/p_{t\ part}$
$3 < p_t < 5\ \text{GeV}$	0.3	0.3
$p_t > 5\ \text{GeV}$	0.3	0.25
	$\eta_{\text{det}} - \eta_{\text{had}}$	$\eta_{\text{had}} - \eta_{\text{part}}$
$3 < p_t < 5\ \text{GeV}$	0.5	0.6
$5 < p_t < 7.5\ \text{GeV}$	0.35	0.4
$p_t > 7.5\ \text{GeV}$	0.2	0.25

which the mean and the width of the Gaussian, the background parameters u_s and, in cases where statistics are very low, u_e are fixed to the values obtained from the fit to the *inclusive D^** sample. The background normalisation u_n is a free parameter.

3.2 Jet selection

In the *inclusive D^** sample jets are defined by the inclusive k_t-algorithm [22] in the p_t-recombination and ΔR-distance scheme (with $R_0 = 1$, [23]). The jet algorithm is applied in the laboratory frame to all reconstructed particles of the HFS. To prevent the decay particles of the D^* candidate from being ascribed to different jets, the D^* candidate is used as a single particle in the jet algorithm, replacing its decay products. In this way the jet containing the D^* meson is unambiguously defined. In events which contain more than one D^* candidate, the jet algorithm is run separately for each candidate. The transverse momentum is required to satisfy $p_t(\text{jet}) > 3\ \text{GeV}$. For jets originating from charm the requirement of $p_t(\text{jet}) > 3\ \text{GeV}$ matches approximately the requirement of $p_t(D^*) > 2\ \text{GeV}$, since the charm fragmentation function to a D^* peaks where the D^* meson takes $\sim 70\%$ of the charm quark momentum [24].

To ensure a good jet reconstruction at these low values of p_t, jets are restricted to the central detector region

$|\eta(\text{jet})| < 1.5$ where precise track information is available. According to Monte Carlo simulations the jets at detector level are found to be well correlated in p_t, η and ϕ to the jets at the hadron and also at the parton level down to low $p_t(\text{jet})$ values. Typical resolutions (RMS) are listed in Table 2.

The jet with the highest $p_t(\text{jet})$ not containing the D^* meson is considered together with the D^* meson in the "$D^* + other\ jet$" analysis. The Δm-distribution of the D^* candidates of this sample is shown in Fig. 2b. A signal of 592 ± 57 D^* mesons is found. In about 10% of the D^* events a second (non-D^*-)jet is observed.

In addition to the $D^* + other\ jet$ sample a "D^* *tagged dijet*" sample is selected. At least two jets are required with $p_t(\text{jet}) > 4\ \text{GeV}$ for the highest p_t jet and $p_t(\text{jet}) > 3\ \text{GeV}$ for the second jet (see Table 1), irrespective of whether the D^* meson is attributed to either of the jets. A signal of 496 ± 53 D^* *tagged dijet* events is observed. The fraction of events where the D^* meson is contained in neither of the two jets is negligible.

4 QCD calculations

Figure 1 shows examples of diagrams for charm photoproduction in leading order $\mathcal{O}(\alpha_s)$ and next-to-leading order $\mathcal{O}(\alpha_s^2)$. In direct-photon processes (Fig. 1a and b), the pho-

ton emitted from the beam lepton enters the hard process directly. In resolved-photon processes (Fig. 1c and d), the photon acts as a source of incoming partons, one of which takes part in the hard interaction. The distinction between these two classes of processes depends on the factorisation scheme and the order in which the calculation is performed.

The data presented in this analysis are compared with leading order (LO) calculations supplemented by parton showers as well as with next-to-leading order (NLO) calculations. The calculations are performed using either the collinear factorisation or the k_t-factorisation approach. The collinear factorisation makes use of the DGLAP [6–10] evolution equations. In this approach transverse momenta obtained through the initial state QCD evolution are neglected and all the transverse momenta are generated in the hard scattering process, i. e. the incoming partons are collinear with the proton, resulting at lowest order in a back-to-back configuration of the heavy quark pair in the transverse plane. Effects from the finite transverse momentum of the gluons enter only at the NLO level (for example in a process like $\gamma g \to c\bar{c}g$ as shown in Fig. 1b). In the k_t-factorisation ansatz the transverse momentum (k_t) of incoming gluons are already included at leading order both in the k_t-dependent off-shell matrix element and the k_t-dependent unintegrated gluon density [25]. Therefore, higher order corrections, i. e. hard parton emissions, are partially considered.

Heavy quark production is calculated either in the massive scheme [26], where heavy quarks are produced only perturbatively via boson–gluon fusion, or in the massless scheme [27], where heavy quarks are treated as massless partons. These two schemes should be appropriate in different regions of phase space [28]: the massive scheme should be reliable when the transverse momentum p_t of the heavy quarks is of similar size compared to m_c, whereas the massless scheme is expected to be valid for $p_t \gg m_c$. Recently, new calculations combining and matching the two approaches in the photoproduction regime have become available [29–31].

The uncertainties on the calculations are estimated by varying the charm quark mass, the renormalisation scale and where possible the factorisation scales. The uncertainty in each bin is obtained by taking the maximal deviations from the central value resulting from the separate variations. The detailed settings are summarised in Table 3. All predictions (except where scale dependent fragmentation functions are used) are based on a D^* fragmentation ratio of $f(c \to D^*) = 0.235$ [39]. The beauty contribution is included in all predictions and amounts to a few percent.

PYTHIA. In *PYTHIA* [40] three different processes are generated separately using leading order matrix-elements: direct photon–gluon fusion (Fig. 1a), resolved photon processes in which a charm quark (charm excitation, Fig. 1c) or a gluon (Fig. 1d) from the photon enters the hard scattering. In the excitation processes the charm quark is treated as a massless parton, whereas in the other processes the charm mass is accounted for in all steps of the calculation. Higher order contributions are simulated with leading log parton showers in the collinear approach. The Lund string fragmentation model [41] is used for the simulation of the hadronisation process. For the longitudinal fragmentation of the charm quark into the D^* meson the Peterson parametrisation [42] is used. No uncertainties are calculated.

CASCADE. The *CASCADE* [43–45] program is used for leading order calculations in the k_t-factorisation approach. In the $\gamma g^* \to c\bar{c}$ matrix element, which takes the charm mass into account, the incoming gluon is treated off mass-

Table 3. Parameters used in the pQCD calculations where m_c denotes the charm quark mass. The "transverse mass" variables are defined as $m_t^2 = m_c^2 + (p_{t,c}^2 + p_{t,\bar{c}}^2)/2$, $m_t^{'2} = 4m_c^2 + p_{t,c}^2$ and $m_{t,D^*}^2 = m_c^2 + p_{t,D^*}^2$ where $p_{t,c}$ ($p_{t,\bar{c}}$) is the transverse momentum of the charm quark (antiquark) and p_{t,D^*} is the transverse momentum of the D^* meson. The squared invariant mass and the transverse momentum squared of the $c\bar{c}$ pair are denoted by $\hat{s}$ and Q_t^2, respectively. ϵ_{pet} is the Peterson fragmentation parameter. If a parameter is varied to determine the uncertainty of the prediction, the central line gives the value used for the main prediction

	PYTHIA	**CASCADE**	**FMNR**	**ZMVFNS**	**GMVFNS**
Version	6.224	1.2010			
Proton PDF	CTEQ6L [32]	A0($\pm$) [33]	CTEQ6M [32]	CTEQ6M	CTEQ6M
Photon PDF	GRV-G LO [34]	–	GRV-G HO [34]	GRV-G HO	GRV-G HO
Renorm. scale	m_t	$\left.\begin{array}{c}2\\1\\0.5\end{array}\right\} \cdot m_t'$	$\left.\begin{array}{c}2\\1\\0.5\end{array}\right\} \cdot m_t$	$\left.\begin{array}{c}2\\1\\-\end{array}\right\} \cdot m_{t,D^*}$	$\left.\begin{array}{c}2\\1\\0.6\end{array}\right\} \cdot m_{t,D^*}$
Factor. scale	m_t	$\sqrt{\hat{s}+Q_t^2}$	$\left.\begin{array}{c}1\\2\\4\end{array}\right\} \cdot m_t$	$\left.\begin{array}{c}1/1.5\\2\\4\end{array}\right\} \cdot m_{t,D^*}$	$\left.\begin{array}{c}0.6\\1\\2\end{array}\right\} \cdot m_{t,D^*}$
m_c [GeV]	1.5	$1.5^{+0.2}_{-0.2}$	$1.5^{+0.2}_{-0.2}$	1.5	1.5
Fragmentation	$\epsilon_{\text{pet}} = 0.04$	$\epsilon_{\text{pet}} = 0.04$	$\epsilon_{\text{pet}} = 0.035$ [35]	BKK O [36]	KKSS [37, 38]

shell and can have a finite transverse momentum. Higher order QCD corrections are simulated with initial state parton showers applying the CCFM evolution [46–49] equations with an unintegrated parton density function (uPDF) including angular ordering constraints for the emitted partons. The uPDF has been obtained from an analysis of the inclusive structure function F_2 in the CCFM approach [33]. For the variation of the renormalisation scale, dedicated unintegrated gluon density parameterisations have been used [33]. The factorisation scale cannot be varied. The final state radiation off the heavy quarks and the fragmentation is performed with *PYTHIA*.

FMNR. The FMNR program [26, 50] implements a massive scheme next-to-leading order calculation ($\mathcal{O}(\alpha_s^2)$) in the collinear factorisation approach. It provides weighted parton level events with two or three outgoing partons, i. e. a $c\bar{c}$ quark pair and possibly one additional light parton. The fragmentation of the charm quarks into D^* mesons is treated by a downscaling of their three-momenta according to the Peterson fragmentation function in a frame where the quark–antiquark pair is back-to-back.

ZMVFNS. The zero-mass variable-flavour-number scheme (ZMVFNS) [27, 51] provides a next-to-leading order calculation ($\mathcal{O}(\alpha_s^2)$) for $D^* + other\ jet$ cross sections in the collinear approach, neglecting the charm mass. The transition from the charm quark to the D^* meson is treated using the scale dependent fragmentation functions determined in [36]. In the determination of the uncertainty the initial and final state factorisation scales are varied simultaneously (with a lowest value of m_{t,D^*} and $1.5\,m_{t,D^*}$, respectively, see Table 3).

GMVFNS. The general-mass variable-flavour-number scheme (GMVFNS) combines the massless with the massive scheme [29–31]. Scale dependent fragmentation functions as determined in [37, 38] are used. The calculation is only available for inclusive D^* production. The initial and final state factorisation scales are varied separately in the uncertainty determination.

For the NLO calculations which are compared to the $D^* + other\ jet$ and $D^*\ tagged\ dijet$ measurements (FMNR and ZMVFNS), additional corrections for hadronisation effects (transition form partons to jets) are applied. These hadronisation corrections are calculated using *PYTHIA*. In *PYTHIA* parton level jets are constructed from the generated quarks and gluons after the parton showers have been simulated. The ratio of hadron and parton level cross sections in each bin is applied to the NLO calculations as a hadronisation correction factor.

5 Results

5.1 Cross section measurement

The bin averaged visible differential cross section with respect to a variable Y (with bin width ΔY) is calculated

according to

$$
\frac{\mathrm{d}\sigma_{\mathrm{vis}}(ep \to e'D^{*\pm}(+\mathrm{jet})X)}{\mathrm{d}Y}
= \frac{N(D^{*\pm}(+\mathrm{jet})) \cdot (1-r)}{\Delta Y \cdot \mathcal{BR}(D^* \to K\pi\pi_s) \cdot \mathcal{L} \cdot \epsilon}\,,
\tag{1}
$$

where a correction $r = 0.035$ [1] is applied to account for reflections within the D^0 mass window, coming from D^0 channels other than the one studied in this analysis. $\mathcal{BR}(D^* \to K\pi\pi_s)$ is the branching ratio of the analysed D^* decay chain and $\mathcal{L}$ is the integrated luminosity. The correction factor ϵ takes into account detector acceptances, trigger and reconstruction efficiencies and migrations between bins. The cross section is defined as the sum of the D^{*+} and D^{*-} cross sections and includes D^* mesons from b-quark decays.

The average acceptance of the electron tagger is calculated as a convolution of the predicted y-distribution with the y-dependent tagger acceptance which is determined as in [52]. The reconstruction and trigger efficiencies as well as the acceptance of the selection criteria are determined using a GEANT 3.15 [53] based simulation of the detector response to events generated with *PYTHIA*. The efficiency of the particle identification using $\mathrm{d}E/\mathrm{d}x$ and of the software filter are deduced from the data.

The following sources of systematic uncertainties (summarised and quantified in Table 4 for the integrated cross section) have been studied:

– The simulation of the trigger signals from the CJCs and the multi-wire proportional chambers have been verified (using data) to within an uncertainty of 4%. Including the efficiency of the software filter this amounts to a 4.5% uncertainty on the cross section measurement.
– The positron beam parameters and the absolute energy scale of the electron tagger have been varied within their uncertainties. The resulting average uncertainty on the tagger acceptance is 5.8%, depending on $W_{\gamma p}$.
– The uncertainty on the track reconstruction efficiency amounts to 6% per D^* meson.
– The uncertainty on the efficiency of the particle identification using $\mathrm{d}E/\mathrm{d}x$ is estimated to be 2% per D^* meson [21].

Table 4. Systematic uncertainties of the integrated cross section measurements

sources	*inclusive* D^* [%]	D^* with jets [%]
trigger efficiency	4.5	
electron tagger acceptance	5.8	
track reconstruction	6	
particle identification	2	
$\mathcal{BR}(D^* \to K\pi\pi_s)$	2.5	
reflections	1.5	
signal extraction	3	
model dependence	1.3	
luminosity $\mathcal{L}$	1.5	
HFS objects energy scale	–	2.8
in total	10.7	11.1

Table 5. Integrated cross section in the visible range for *inclusive D^**, *D^* + other jet* and *D^* tagged dijet* photoproduction. For the cross sections for processes involving jets the result of the NLO calculations before the correction for hadronisation effects is given in brackets

$\sigma_{\rm vis}$ [nb] Data	inclusive D^* $6.45 \pm 0.46 \pm 0.69$	D^* + other jet $3.01 \pm 0.29 \pm 0.33$	D^* tagged dijet $2.32 \pm 0.25 \pm 0.26$
FMNR	$5.9^{+2.8}_{-1.3}$	$\left(2.65^{+0.78}_{-0.42}\right)$	$\left(2.44^{+0.97}_{-0.52}\right)$
$\otimes$ had. corr.		$2.35^{+0.69}_{-0.37}$	$2.09^{+0.83}_{-0.44}$
ZMVFNS	–	$\left(3.05^{+0.62}_{-0.47}\right)$	–
$\otimes$ had. corr.		$2.71^{+0.55}_{-0.42}$	–
GMVFNS	$8.2^{+5.3}_{-4.0}$	–	–
PYTHIA	8.9	3.8	2.8
CASCADE	$5.38^{+0.54}_{-0.62}$	$3.08^{+0.22}_{-0.28}$	$2.48^{+0.17}_{-0.20}$

– The uncertainty on the D^* branching ratio is 2.5% [20].
– The uncertainty on the correction for reflections from other D^0 decays is 1.5% [1].
– The uncertainty on the extraction of the D^* signal from the Δm distributions has been determined in [21] and amounts to 3%.
– The model dependence of the correction factors is estimated by using *CASCADE* instead of *PYTHIA*. Half of the resulting deviation is taken as the uncertainty on the signal extraction procedure, i. e. 1.3% for the total *inclusive D^** sample and up to 17% for the differential distributions.
– The luminosity is determined with a precision of 1.5%.
– The uncertainty on the energy of the HFS objects leads to a systematic uncertainty on the D^*-jet cross sections of 2.8%.

The total systematic uncertainty is obtained by adding each uncertainty in quadrature and amounts to 11% for the integrated cross sections and up to 20% for differential distributions.

5.2 Inclusive D^* cross sections

The integrated D^* photoproduction cross section is measured to be:

$$\sigma_{\rm vis}(ep \to e'D^{*\pm}X) = 6.45 \pm 0.46\,({\rm stat.}) \pm 0.69\,({\rm sys.})\ {\rm nb},$$

in the visible range given by $0.29 < y < 0.65$, $Q^2 < 0.01\ {\rm GeV}^2$, $p_{\rm t}(D^*) > 2\ {\rm GeV}$ and $|\eta(D^*)| < 1.5$. In Table 5 the predictions from QCD calculations are listed and compared with this measurement. The central values from FMNR and *CASCADE* are slightly lower than the measured result, whereas those of *PYTHIA* and GMVFNS are higher.

The measured bin averaged differential cross sections are shown in Figs. 3–5 and given in Tables 6 and 7. The predictions show large uncertainties compared with those on the data. These uncertainties partially cancel in the comparison of the shapes of the distributions. The
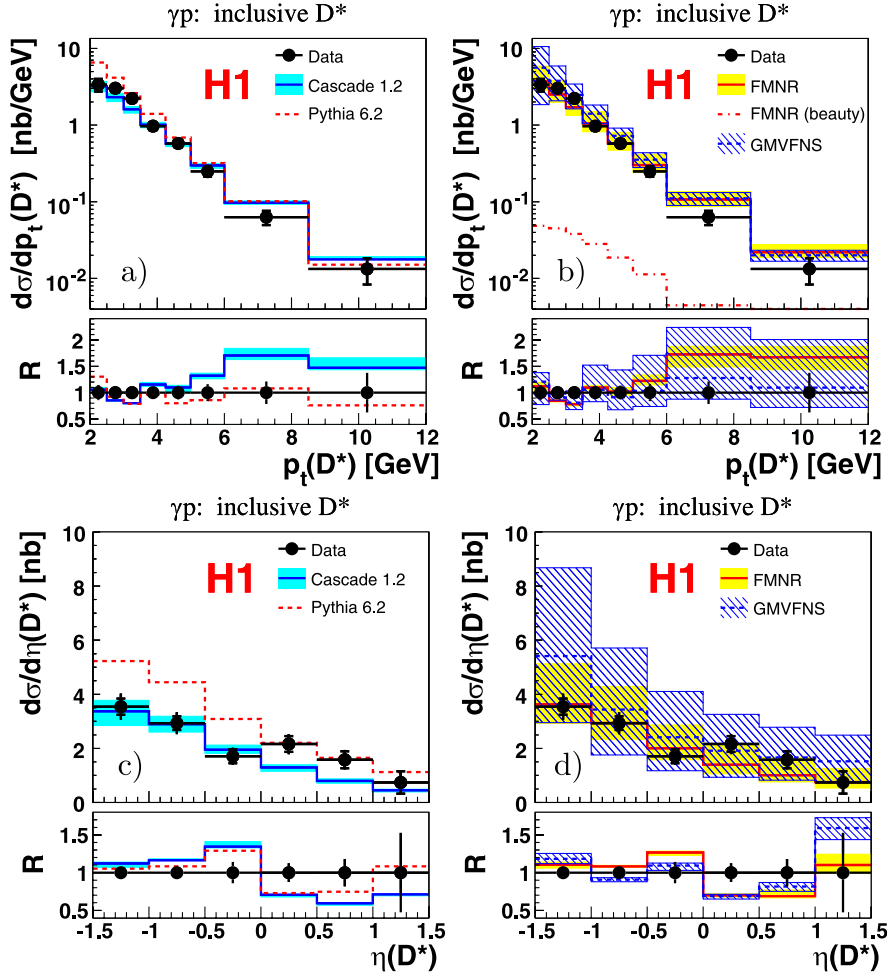
Table 6. Bin averaged differential cross sections for *inclusive D^** production in bins of $p_{\rm t}(D^*)$, $\eta(D^*)$, $z(D^*)$ and $W_{\gamma p}$ with their statistical and systematical uncertainties

Inclusive D^* Cross Sections			
$p_{\rm t}(D^*)$ range [GeV]	${\rm d}\sigma/{\rm d}p_{\rm t}(D^*)$ 	stat. [nb/GeV]	sys.
2.0 2.5	3.37	0.63	0.36
2.5 3.0	3.01	0.37	0.32
3.0 3.5	2.22	0.23	0.24
3.5 4.25	0.97	0.11	0.10
4.25 5.0	0.577	0.071	0.063
5.0 6.0	0.250	0.038	0.027
6.0 8.5	0.063	0.013	0.0068
8.5 12.0	0.0133	0.0050	0.0016
$\eta(D^*)$ range	${\rm d}\sigma/{\rm d}\eta(D^*)$ [nb]	stat.	sys.
−1.5 −1.0	3.54	0.30	0.38
−1.0 −0.5	2.93	0.25	0.31
−0.5 0.0	1.71	0.26	0.19
0.0 0.5	2.16	0.29	0.23
0.5 1.0	1.58	0.31	0.18
1.0 1.5	0.74	0.41	0.08
$z(D^*)$ range	${\rm d}\sigma/{\rm d}z(D^*)$ [nb]	stat.	sys.
0 0.1	10.8	2.5	1.2
0.1 0.2	17.8	1.9	2.0
0.2 0.3	9.9	1.2	1.1
0.3 0.45	8.66	0.76	0.93
0.45 0.6	6.00	0.58	0.64
0.6 0.8	1.48	0.24	0.19
$W_{\gamma p}$ range [GeV]	${\rm d}\sigma/{\rm d}W_{\gamma p}$ [nb/GeV]	stat.	sys.
172 192	0.112	0.012	0.017
192 212	0.0784	0.0077	0.0077
212 232	0.0601	0.0071	0.0058
232 256	0.0548	0.0078	0.0057

ratio

$$R = \frac{\frac{1}{\sigma_{\rm vis}^{\rm calc}} \frac{{\rm d}\sigma^{\rm calc}}{{\rm d}Y}}{\frac{1}{\sigma_{\rm vis}^{\rm data}} \frac{{\rm d}\sigma^{\rm data}}{{\rm d}Y}} \qquad (2)$$

Fig. 3. Inclusive D^* cross sections as a function of $p_t(D^*)$ (**a,b**) and $\eta(D^*)$ (**c,d**) compared with the predictions of *PYTHIA* and *CASCADE on the left* and of the next-to-leading order calculations FMNR and GMVFNS *on the right*. For FMNR the beauty contribution is shown separately for $p_t(D^*)$. Here and in the following figures the *inner error bars* indicate the statistical errors and the *outer error bars* show the statistical and systematic uncertainties added in quadrature. The normalised ratio R (2) is also shown

Table 7. Bin averaged differential cross sections for *inclusive* D^* production in bins of $\eta(D^*)$ for three ranges in $p_t(D^*)$ with their statistical and systematical uncertainties

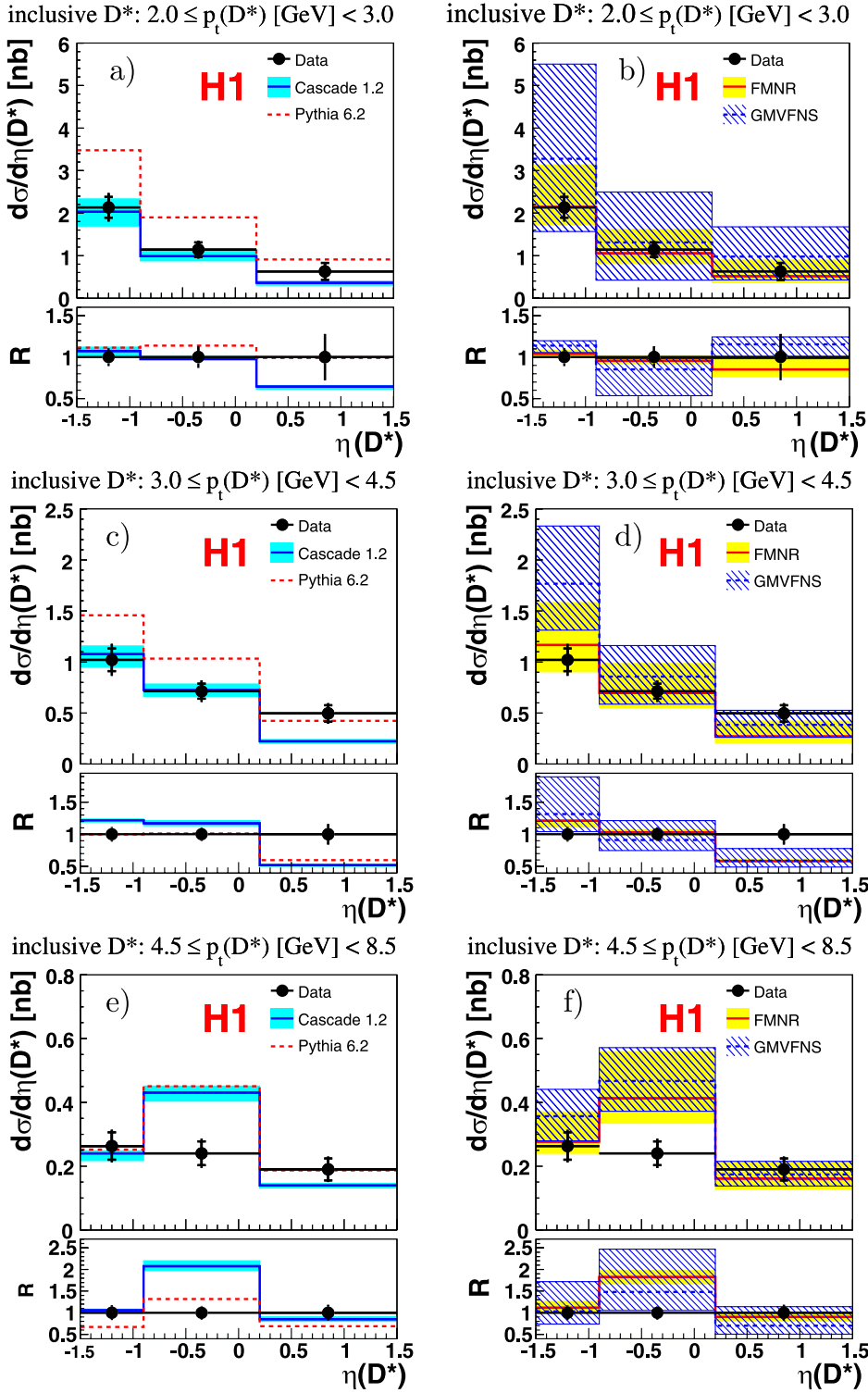| Inclusive D^* Cross Sections			
$2.0 \leq p_t(D^*) < 3.0\,\mathrm{GeV}$			
$\eta(D^*)$ range	$d\sigma/d\eta(D^*)$ [nb]	stat.	sys.
$-1.5 \quad -0.9$	2.14	0.25	0.23
$-0.9 \quad 0.2$	1.14	0.17	0.12
$0.2 \quad 1.5$	0.63	0.20	0.07
$3.0 \leq p_t(D^*) < 4.5\,\mathrm{GeV}$			
$\eta(D^*)$ range	$d\sigma/d\eta(D^*)$ [nb]	stat.	sys.
$-1.5 \quad -0.9$	1.02	0.11	0.11
$-0.9 \quad 0.2$	0.714	0.073	0.077
$0.2 \quad 1.5$	0.495	0.082	0.057
$4.5 \leq p_t(D^*) < 8.5\,\mathrm{GeV}$			
$\eta(D^*)$ range	$d\sigma/d\eta(D^*)$ [nb]	stat.	sys.
$-1.5 \quad -0.9$	0.263	0.043	0.028
$-0.9 \quad 0.2$	0.240	0.037	0.027
$0.2 \quad 1.5$	0.190	0.034	0.020

is therefore also presented, where Y denotes any measured variable. Note that here each differential cross section is normalised to its own visible cross section (*inclusive D^*, D^* + other jet* or *D^* tagged dijet*).

In Fig. 3a and b the cross section is shown differentially in the transverse momentum of the D^*. The cross section falls steeply with increasing $p_t(D^*)$ as predicted by all calculations. *CASCADE* and FMNR predict a distribution which falls less steeply at large $p_t(D^*)$ than is visible in the data. The *PYTHIA* and GMVFNS calculations describe the slope well. However, the theoretical uncertainty of the GMVFNS calculations is large. In Fig. 3b the small contribution coming from b-decays as determined from FMNR is shown separately.

In Fig. 3c and d the differential cross section is shown as a function of the pseudorapidity $\eta(D^*)$. The cross section decreases with increasing η (the forward direction $\eta > 0$). All calculations predict a similar shape, differing from that in the data, which shows a larger relative contribution in the forward direction.

In Fig. 4 the differential cross section is shown as a function of $\eta(D^*)$ for three bins in $p_t(D^*)$. As for the inclusive $\eta(D^*)$ distribution none of the calculations is able to describe the data completely.

The inelasticity $z(D^*)$, defined by $z(D^*) = Pp(D^*)/(Pq)$ with P, $p(D^*)$ and q being the four-momenta of the incoming proton, the D^* meson and the exchanged photon, is a measure of the fraction of photon energy transferred to the D^* meson in the proton rest frame. This quantity

Fig. 4. Inclusive D^* cross sections as a function of $\eta(D^*)$ for three bins of $p_{\mathrm{t}}(D^*)$ compared with the predictions of *PYTHIA* and *CASCADE on the left* and of the next-to-leading order calculations FMNR and GMVFNS *on the right*

is sensitive to the production mechanism and to the $c \to D^*$ fragmentation function. It is reconstructed as $z(D^*) = (E - p_z)_{D^*}/(2yE_e)$. The differential cross section as a function of $z(D^*)$ is compared to the predictions in Fig. 5a and b. For $z(D^*) > 0.2$ the *CASCADE* and FMNR predictions agree fairly well with the data. However, in both cases the predictions (central values) underestimate the measured cross section in the region $z(D^*) < 0.2$. A similar finding

is reported for a measurement of D^* production in deep inelastic scattering ($Q^2 > 1\,\mathrm{GeV}^2$) [54]. *PYTHIA* can account for the large cross section at small $z(D^*)$, but overestimates the cross section at medium $z(D^*)$. The central value of the GMVFNS calculation is slightly higher than the measurement, but the uncertainties cover the whole range. None of the calculations describes the overall shape of the data.
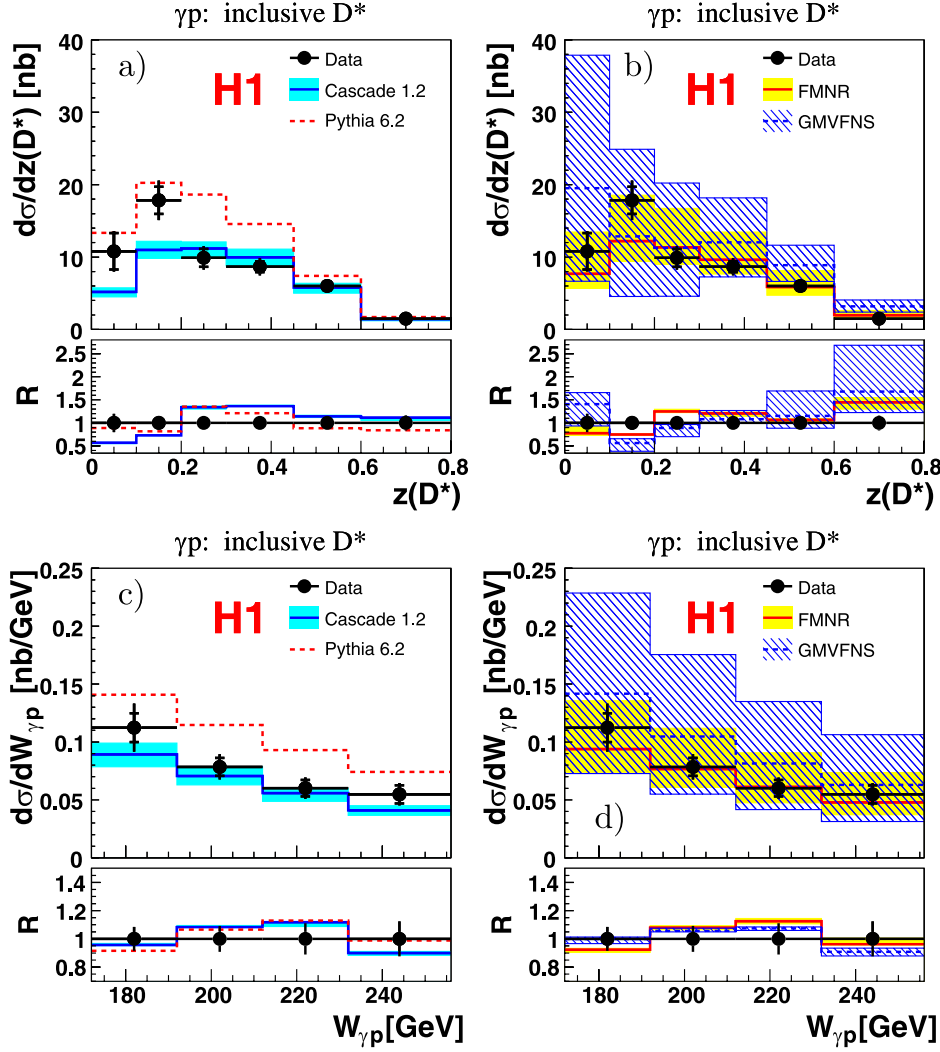
Fig. 5. Inclusive D^* cross sections as a function of the inelasticity $z(D^*)$ (**a,b**) and the photon-proton centre-of-mass energy $W_{\gamma p}$ (**c,d**) compared with the predictions of *PYTHIA* and *CASCADE on the left* and of the next-to-leading order calculations FMNR and GMVFNS *on the right*

The cross section as a function of $W_{\gamma p}$ is shown in Fig. 5c and d. It falls weakly with increasing $W_{\gamma p}$. The behaviour observed in the data is reproduced by all calculations within the uncertainties.

In summary, significant differences are observed in the shape of most of the distributions between data and all central theoretical predictions. A good agreement is only found for the $W_{\gamma p}$ distribution for which each bin receives contributions throughout the available phase space of the produced $D^{*\pm}$ meson. Here all calculations predict very similar shapes. For those observables which are especially sensitive to the phase space distribution of the outgoing charm quark, i.e. $p_t(D^*)$, $\eta(D^*)$ and $z(D^*)$, large deviations in shape between data and theory are observed. It is interesting to observe that the cross sections predicted by the calculations which treat the heavy quark mass explicitly (*CASCADE* and FMNR) are similar.

5.3 D^* + other jet and D^* tagged dijet cross sections

A more detailed investigation of the heavy quark production process is performed by analysing events with a $D^{*\pm}$ meson with either a jet not containing the D^* (D^* + *other jet*) or with two jets (D^* *tagged dijet*). In this way one can tag a second outgoing parton from the hard interaction in addition to the (anti-)charm quark. The requirements for the D^* meson and the photoproduction selection are the same as in the inclusive case. In the D^* + *other jet* analysis the jet is required to have a transverse momentum $p_t(\text{jet}) > 3\,\text{GeV}$ in the range of $|\eta(\text{jet})| < 1.5$ in the laboratory frame. The integrated (D^* + *other jet*) cross section in the visible range given in Table 1 is measured to be

$$\sigma_{\text{vis}}(ep \to e'D^{*\pm} + \text{other jet } X)$$
$$= 3.01 \pm 0.29\,(\text{stat.}) \pm 0.33\,(\text{sys.})\,\text{nb}.$$

The integrated D^* *tagged dijet* cross section ($p_t(\text{jet}) > 4(3)\,\text{GeV}$, $|\eta(\text{jet})| < 1.5$) is measured to be (in the visible range given in Table 1)

$$\sigma_{\text{vis}}(ep \to e'D^{*\pm} + 2\,\text{jet } X)$$
$$= 2.32 \pm 0.25\,(\text{stat.}) \pm 0.26\,(\text{sys.})\,\text{nb}.$$

In Table 5 both values are compared with the predictions from the QCD calculations. All predictions agree with the

Table 8. Bin averaged differential cross sections for the D^* + *other jet* sample in bins of $p_t(D^*)$, $p_t(\text{jet})$, $\eta(D^*)$, $\eta(\text{jet})$ and $\eta(D^*)$ - $\eta(\text{jet})$ with their statistical and systematical uncertainties. The last column shows the hadronisation correction factors applied to the NLO calculations

D^* + other jet Cross Sections					
$p_t(D^*)$ range [GeV]		$d\sigma/dp_t(D^*)$ [nb/GeV]	stat.	sys.	f_{had}
2.0	3.5	1.35	0.16	0.15	0.87
3.5	5.0	0.407	0.051	0.044	0.92
5.0	7.5	0.124	0.017	0.014	0.96
7.5	11.0	0.0116	0.0048	0.0013	0.97
$p_t(\text{jet})$ range [GeV]		$d\sigma/dp_t(\text{jet})$ [nb/GeV]	stat.	sys.	f_{had}
3.0	5.0	0.870	0.094	0.095	0.91
5.0	7.5	0.334	0.049	0.037	0.85
7.5	11.0	0.084	0.021	0.010	0.85
11.0	16.0	0.0201	0.0071	0.0022	0.91
$\eta(D^*)$ range		$d\sigma/d\eta(D^*)$ [nb]	stat.	sys.	f_{had}
−1.5	−1.0	1.46	0.18	0.16	0.86
−1.0	−0.5	1.46	0.17	0.16	0.89
−0.5	0.1	0.99	0.16	0.11	0.90
0.1	0.8	1.05	0.18	0.12	0.91
0.8	1.5	0.33	0.22	0.04	0.90
$\eta(\text{jet})$ range		$d\sigma/d\eta(\text{jet})$ [nb]	stat.	sys.	f_{had}
−1.5	−1.0	0.84	0.16	0.092	0.66
−1.0	−0.5	1.15	0.19	0.13	0.90
−0.5	0.1	1.15	0.18	0.13	0.94
0.1	0.8	0.84	0.17	0.093	0.99
0.8	1.5	0.99	0.17	0.11	0.94
$\eta(D^*)$ - $\eta(\text{jet})$ range		$d\sigma/d(\eta(D^*)$ - $\eta(\text{jet}))$ [nb]	stat.	sys.	f_{had}
−2.8	−1.9	0.318	0.065	0.037	1.01
−1.9	−1.0	0.66	0.10	0.07	0.98
−1.0	0.0	1.01	0.13	0.11	0.86
0.0	1.0	0.63	0.13	0.07	0.81
1.0	1.9	0.44	0.11	0.05	0.88
1.9	2.8	0.084	0.071	0.012	0.89

measurements within the quoted calculated uncertainties, including ZMVFNS for the D^* + *other jet* sample.

The bin averaged differential cross section for the D^* + *other jet* and D^* *tagged dijet* are listed in Tables 8 and 9 and shown in Figs. 6–9. The cross sections for the D^* + *other jet* selection are shown in Fig. 6 as functions of $p_t(D^*)$ and $p_t(\text{jet})$ together with theoretical predictions. The calculations overestimate the cross section at large $p_t(D^*)$, while the cross section as a function of $p_t(\text{jet})$ is well described by the NLO calculations. *CASCADE* overestimates the cross sections at large $p_t(\text{jet})$.

Cross sections as a function of $\eta(D^*)$ and $\eta(\text{jet})$ are shown in Fig. 7a–d. They differ noticeably: The $\eta(D^*)$ distribution falls steeply with increasing values of η (similar to the inclusive case), whereas $\eta(\text{jet})$ is almost flat. For direct photon–gluon fusion processes ($\gamma g \to c\bar{c}$), as shown separately for *PYTHIA*, the shapes of the cross sections as a function of $\eta(D^*)$ and $\eta(\text{jet})$ are found to be similar (dotted lines in Fig. 7a and c), indicating that the difference is not caused by the slightly different kinematic cuts for the

D^* and the jet. The observed difference in shape between the $\eta(D^*)$ and $\eta(\text{jet})$ distributions indicates the presence of hard non-charm partons in the forward region. In fact, the dominant mechanism for non-charm jets, as predicted by the calculations, is hard gluon radiation off the gluon from the proton, either calculated as an NLO correction (Fig. 1b), as a (LO) charm excitation (Fig. 1c) or by using an unintegrated gluon density. All calculations include this diagram and can describe the observed shapes of $\eta(D^*)$ and $\eta(\text{jet})$ in general.

The D^* + *other jet* measurement allows the investigation of correlations between the D^* and the jet. The cross section as a function of $\eta(D^*)$ - $\eta(\text{jet})$ is shown in Fig. 7e and f. The distribution is not symmetric but the jet is on average more forward than the D^*. The cross section is reasonably well described in shape and magnitude by all QCD calculations.

In collinear factorisation at LO a resolved photon process is characterised by $x_\gamma < 1$, where x_γ is the fraction of the longitudinal photon momentum entering the hard scattering process. In the D^* *tagged dijet* sample, x_γ is ex-

Table 9. Bin averaged differential cross sections for the D^* *tagged dijet* sample in bins of x_γ^{obs} and the $D^* + other\ jet$ cross section as a function of $\Delta\phi(D^*, \mathrm{jet})$ with their statistical and systematical uncertainties. The last column shows the hadronisation correction factors applied to the NLO calculations

D^* **tagged dijet Cross Sections**					
x_γ^{obs} range		$\mathrm{d}\sigma/\mathrm{d}x_\gamma^{\mathrm{obs}}$	stat.	sys.	f_{had}
			[nb]		
0.0	0.3	0.60	0.39	0.12	0.69
0.3	0.6	2.23	0.45	0.36	0.88
0.6	0.8	2.12	0.51	0.27	1.40
0.8	1.0	4.81	0.44	0.53	0.68
$D^* +$ **other jet Cross Sections**					
$\Delta\phi(D^*, \mathrm{jet})$ range		$\mathrm{d}\sigma/\mathrm{d}\Delta\phi(D^*, \mathrm{jet})$	stat.	sys.	f_{had}
[°]			[nb/°]		
0	86	0.00167	0.00086	0.00022	0.62
86	114	0.0108	0.0029	0.0012	0.91
114	138	0.0156	0.0040	0.0018	0.91
138	154	0.034	0.0062	0.0039	0.94
154	170	0.0561	0.0077	0.0061	0.90
170	180	0.073	0.010	0.008	0.91
154	180	0.0625	0.0061	0.0068	0.91
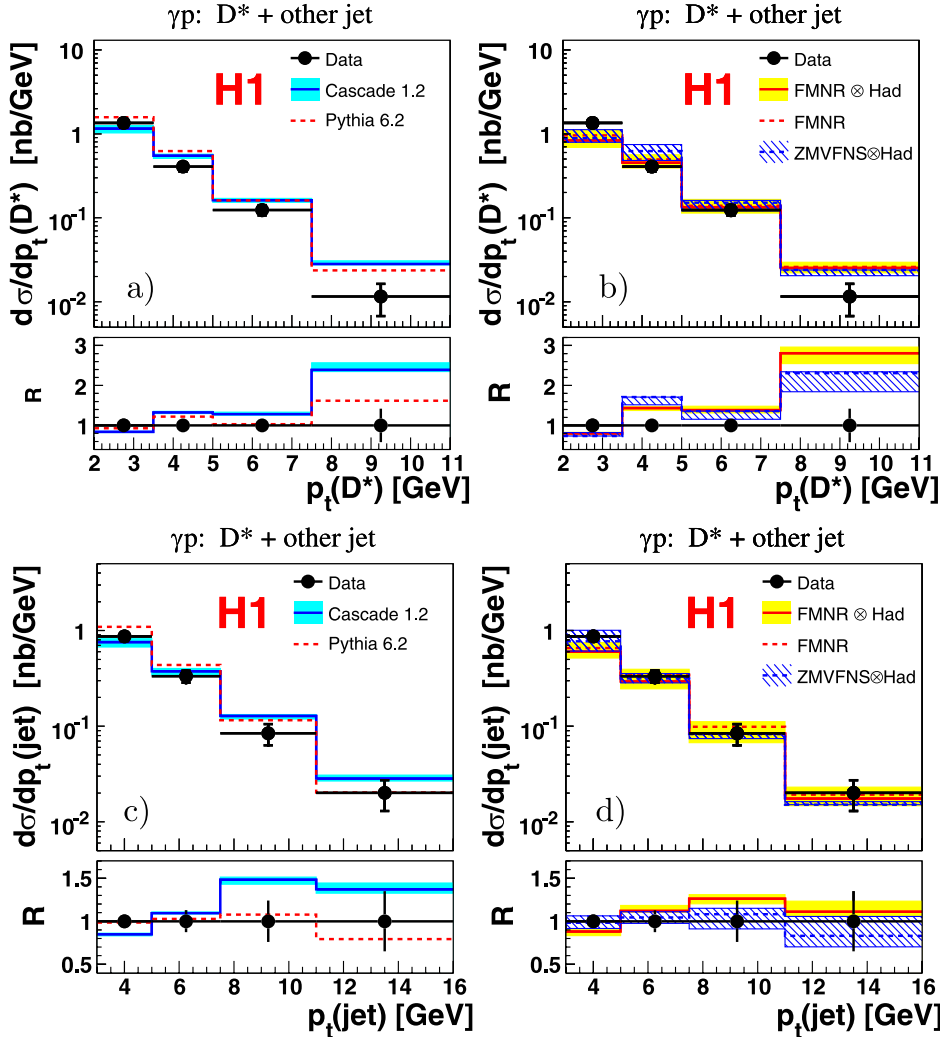
Fig. 6. $D^* + other\ jet$ cross sections as a function of the transverse momenta of the D^* and the jet compared with the predictions of *PYTHIA* and *CASCADE on the left* and of the next-to-leading order calculations FMNR and ZMVFNS *on the right*. Here and in the following figures the central FMNR prediction is shown before and after applying the hadronisation corrections for the jet
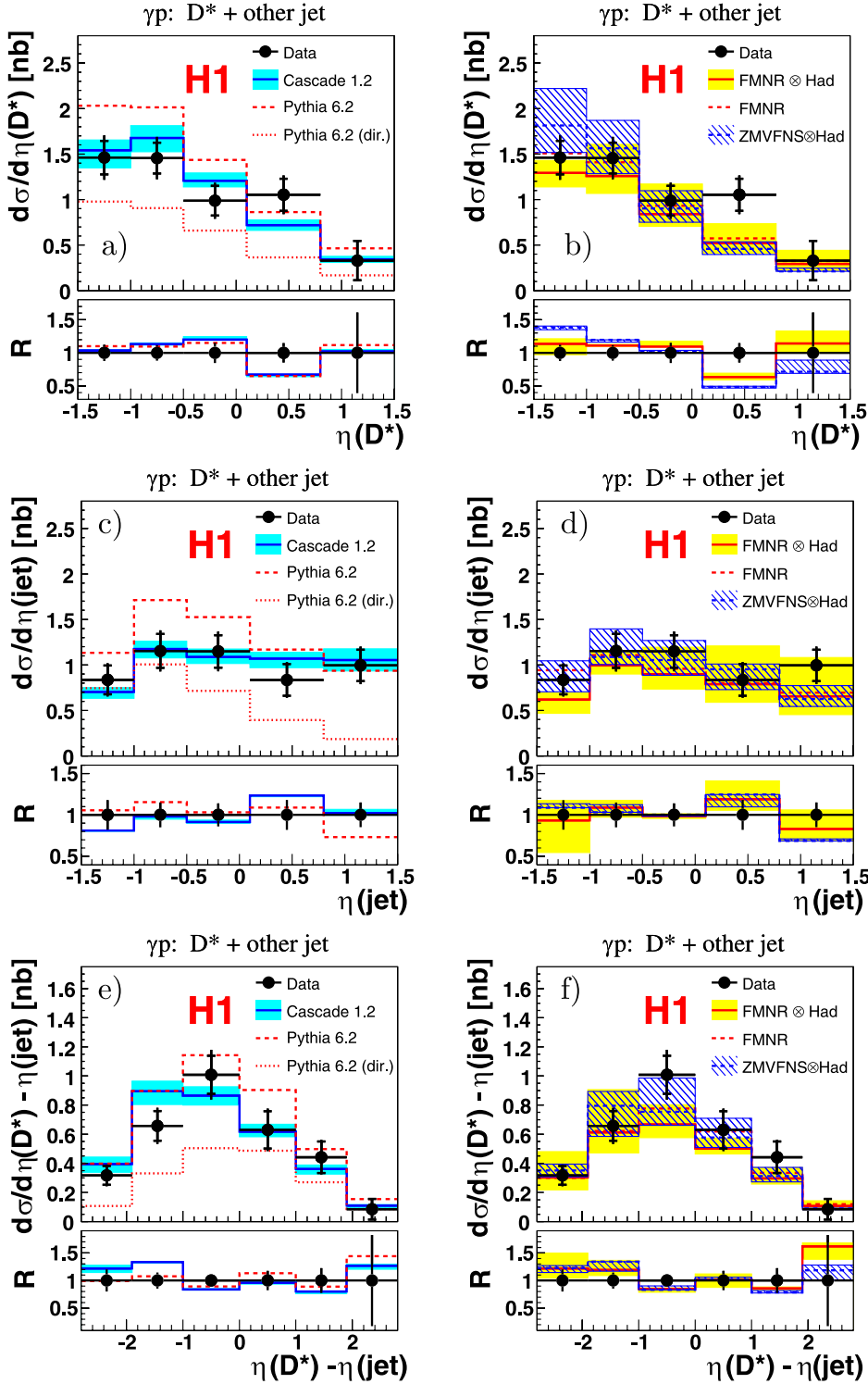
Fig. 7. $D^* + other\ jet$ cross sections as a function of the $\eta(D^*)$ and $\eta(\text{jet})$ and of their difference, compared with the predictions of *PYTHIA* and *CASCADE* (*left*) and of the NLO calculations FMNR and ZMVFNS (*right*). Here and in the following figures the direct photon contribution of *PYTHIA* is shown separately and labelled "PYTHIA 6.2 (dir.)"

perimentally approximated by

$$x_\gamma^{\text{obs}} = \frac{\sum_{i=1}^{\text{jet1+jet2}}(E-p_z)_i}{\sum_{j=1}^{\text{all}}(E-p_z)_j}\,. \tag{3}$$

The sum in the numerator includes the particles in the two selected jets, whereas the sum in the denominator contains all reconstructed particles of the hadronic final state. At

NLO x_γ^{obs} is sensitive to $\mathcal{O}(\alpha_s^2)$ contributions. In the k_{t}-factorisation approach the x_γ^{obs} observable is sensitive to the contribution from gluon emission in the initial state.

The D^* *tagged dijet* cross section as a function of x_γ^{obs} is shown in Fig. 8. The large cross section at small x_γ^{obs} shows that processes beyond direct photon–gluon fusion are needed to describe the data in the collinear approach
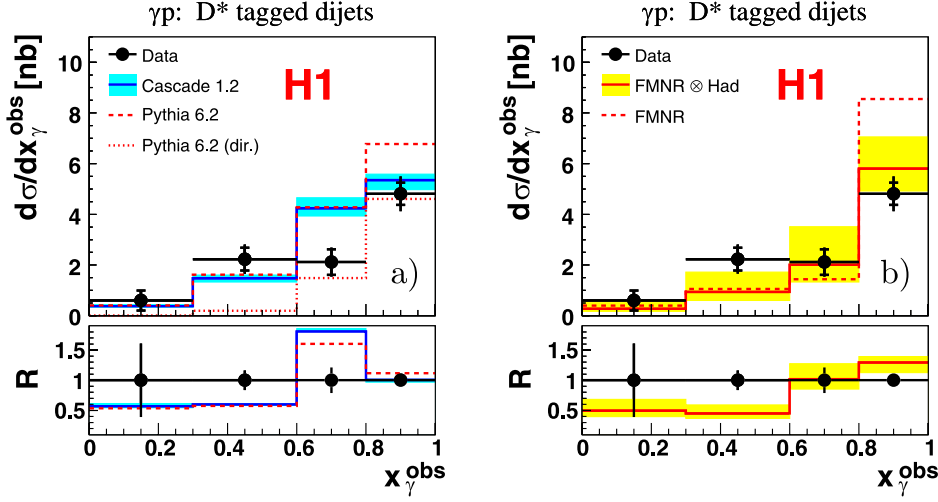
Fig. 8. D^* *tagged dijet* cross sections as a function of x_γ^{obs} compared with the predictions of *PYTHIA* and *CASCADE on the left* and of the next-to-leading order calculation FMNR *on the right*

(as can be seen by comparison with the prediction from *PYTHIA* (dir.) in Fig. 8a.). Both *PYTHIA* and *CASCADE* give a poor description of the x_γ^{obs} distribution. All predictions underestimate the region of low $x_\gamma^{\mathrm{obs}} < 0.6$ which can be clearly seen in the normalised shape R. The hadronisation corrections applied to the FMNR calculation are large.

The correlation in the transverse plane is experimentally accessed by the difference in the azimuthal angle $\Delta\phi(D^*, \mathrm{jet})$ between the D^* and the jet in the $D^* + other\ jet$ sample. The cross section as a function of $\Delta\phi(D^*, \mathrm{jet})$ is shown in Fig. 9. Only $\sim 25\%$ of the measured cross section originates from a back-to-back configuration in the transverse plane with $\Delta\phi(D^*, \mathrm{jet}) > 170°$. Such a configuration is expected for the process $\gamma g \to c\bar{c}$ in the collinear approximation. The large fraction of events where the D^* and the jet are not back-to-back can only be described by models which include significant contributions from higher order QCD radiation.

In *PYTHIA* higher order contributions are simulated by leading log parton showers and the charm excitation process. In *CASCADE* higher order contributions lead to

a significant k_{t} of the gluon entering the hard subprocess as simulated by the unintegrated gluon density. The large deviations from the back-to-back topology are well described by both *PYTHIA* and *CASCADE*. The back-to-back configuration is overestimated by *PYTHIA*, while with the given parameterisation of the unintegrated gluon density *CASCADE* tends to underestimate the back-to-back region and overestimates the small $\Delta\phi(D^*, \mathrm{jet})$ configuration which corresponds to large k_{t}. It is interesting to note that *CASCADE* also predicts significantly harder p_{t} spectra than that observed in the data for the *inclusive D^** cross section in Fig. 3a as well as for the D^* and jet cross sections in Fig. 6a and c for the $D^* + other\ jet$ sample. These quantities are also sensitive to the k_{t} of the gluon which suggests that the current unintegrated gluon density is too hard in k_{t}.

In the NLO calculations $\Delta\phi(D^*, \mathrm{jet}) \neq 180°$ comes entirely from real gluon emission ($\gamma g \to c\bar{c}g$) and from processes initiated by light quarks from the proton ($\gamma q \to c\bar{c}q$). The NLO calculations, although $\mathcal{O}(\alpha_s^2)$, include only the lowest order contribution to this region. The NLO calculations are in reasonable agreement with the measurement in the region of $\Delta\phi(D^*, \mathrm{jet}) > 120°$, but show large discrep-
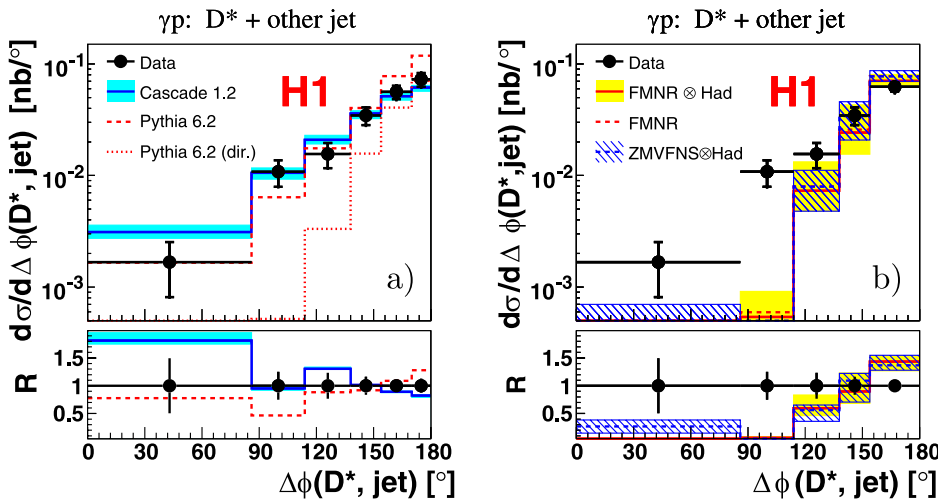
Fig. 9. D^*+jet cross sections as function of $\Delta\phi(D^*, \mathrm{jet})$ compared with the predictions of *PYTHIA* and *CASCADE on the left* and of the next-to-leading order calculations FMNR and ZMVFNS *on the right*. Due to divergencies in the NLO calculations the last two bins of (**a**) are merged in (**b**)

ancies for $\Delta\phi(D^*, \text{jet}) < 120°$, suggesting the presence of higher order contributions. A similar behaviour was found in the measurement of D^* dijet data by the ZEUS collaboration [4] where significantly higher transverse momenta of the jets were required.

6 Conclusions

The photoproduction of D^* mesons is investigated with the H1 detector at HERA using a data sample five times larger than in a previous publication.

Differential cross sections are determined for events with a D^* meson (*inclusive D^**) and for events with a D^* meson and jets (*$D^* + other jet$* and *D^* tagged dijet*). Jets are selected with transverse momenta down to 3 GeV. The results are compared with QCD calculations based on different approaches in leading and next-to-leading order pQCD employing either collinear or k_t-factorisation.

The precision of the *inclusive D^** cross section measurements presented here is much higher than the accuracy of the NLO calculations. The comparison of normalised cross sections, for which these theoretical uncertainties are significantly reduced, reveals sizable differences between data and theoretical predictions for variables sensitive to the phase space distribution of the outgoing charm quark. However, a good agreement is found for the $W_{\gamma p}$ distribution for which each bin receives contributions throughout the available phase space of the produced $D^{*\pm}$ meson.

In the *$D^* + other jet$* analysis a jet is required in addition which does not contain the D^* meson. In general the predictions agree better with the measurements than is the case for the *inclusive D^** analysis. The cross section as a function of $\eta(\text{jet})$ is almost flat in contrast to the cross section as a function of $\eta(D^*)$ which falls towards increasing $\eta(D^*)$. This indicates the presence of jets originating from non-charmed partons, most likely from gluons. All calculations are able to reproduce this feature of the data. Correlations between the D^* and the jet in the transverse plane are investigated by measurements of the difference in azimuthal angle $\Delta\phi(D^*, \text{jet})$. A large fraction of the produced D^*+jet combinations deviates from a back-to-back configuration, indicating the importance of higher order contributions. The large tails of the $\Delta\phi(D^*, \text{jet})$ distribution can be reproduced reasonably well by LO calculations in the collinear factorisation ansatz which include parton showers and charm excitation processes and by using unintegrated gluon densities in the k_t-factorisation ansatz. However, there are differences in shape observed between the data and these predictions. Especially for *CASCADE* the $\Delta\phi(D^*, \text{jet})$ distribution, together with the distributions in $p_t(D^*)$ and $p_t(\text{jet})$, suggests that the unintegrated gluon density used for this analysis overestimates the high k_t region. The available NLO calculations underestimate significantly the observed cross sections in the region $\Delta\phi(D^*, \text{jet}) < 120°$.

In the *D^* tagged dijet* analysis two jets are required in addition to the D^* meson and the observable x_γ^{obs} is studied. All calculations underestimate the cross section in the region of low $x_\gamma^{\text{obs}} < 0.6$ where resolved photon processes or other higher order contributions are expected to be enhanced.

References

1. H1 Collaboration, C. Adloff et al., Nucl. Phys. B **545**, 21 (1999) [hep-ex/9812023]
2. ZEUS Collaboration, J. Breitweg et al., Eur. Phys. J. C **6**, 67 (1999) [hep-ex/9807008]
3. ZEUZ Collaboration, S. Chekanov et al., Phys. Lett. B **565**, 87 (2003) [hep-ex/0302025]
4. ZEUS Collaboration, S. Chekanov et al., Nucl. Phys. B **729**, 492 (2005) [hep-ex/0507089]
5. H1 Collaboration, A. Aktas et al., Phys. Lett. B **621**, 56 (2005) [hep-ex/0503038]
6. V.N. Gribov, L.N. Lipatov, Sov. J. Nucl. Phys. **15**, 438 (1972)
7. V.N. Gribov, L.N. Lipatov, Sov. J. Nucl. Phys. **15**, 675 (1972)
8. L.N. Lipatov, Sov. J. Nucl. Phys. **20**, 94 (1975)
9. G. Altarelli, G. Parisi, Nucl. Phys. B **126**, 298 (1977)
10. Y.L. Dokshitzer, Sov. Phys. JETP **46**, 641 (1977)
11. L.V. Gribov, E.M. Levin, M.G. Ryskin, Phys. Rep. **100**, 1 (1983)
12. E.M. Levin, M.G. Ryskin, Y.M. Shabelski, A.G. Shuvaev, Sov. J. Nucl. Phys. **53**, 657 (1991)
13. S. Catani, M. Ciafaloni, F. Hautmann, Nucl. Phys. B **366**, 135 (1991)
14. J.C. Collins, R.K. Ellis, Nucl. Phys. B **360**, 3 (1991)
15. H1 Collaboration, I. Abt et al., Nucl. Instrum. Methods A **386**, 310 (1997)
16. H1 Collaboration, I. Abt et al., Nucl. Instrum. Methods A **386**, 348 (1997)
17. D. Pitzl et al., Nucl. Instrum. Methods A **454**, 334 (2000) [hep-ex/0002044]
18. J. Steinhart, Die Messung des totalen $c\bar{c}$-Photoproduktions-Wirkungsquerschnittes durch die Rekonstruktion von Λ_c Baryonen unter Verwendung der verbesserten dE/dx Teilchenidentifikation am H1 Experiment bei HERA. Ph.D. Thesis, Universität Hamburg, Report DESY-THESIS-1999-029, Apr. 1999. Available at https://www-h1.desy.de/publications/theses_list.html
19. H1 SPACAL Group, R.D. Appuhn et al., Nucl. Instrum. Methods A **386**, 397 (1997)
20. Particle Data Group, S. Eidelman et al., Phys. Lett. B **592**, 1 (2004)
21. G. Flucke, Photoproduction of D^* Mesons and D^* Mesons Associated with Jets at HERA, Ph.D. Thesis, Universität Hamburg, Report DESY-THESIS-2005-006, Mar. 2005. Available at https://www-h1.desy.de/publications/theses_list.html

22. S. Ellis, D. Soper, Phys. Rev. D **48**, 3160 (1993) [hep-ph/9305266]
23. J.M. Butterworth, J.P. Couchman, B.E. Cox, B.M. Waugh, Comput. Phys. Commun. **153**, 85 (2003) [hep-ph/0210022]
24. CLEO Collaboration, M. Artuso et al., Phys. Rev. D **70**, 112001 (2004) [hep-ex/0402040]
25. J. Collins, H. Jung, *Need for Fully Unintegrated Parton Densities*, 2005 [hep-ph/0508280]
26. S. Frixione, P. Nason, G. Ridolfi, Nucl. Phys. B **454**, 3 (1995) [hep-ph/9506226]
27. B.A. Kniehl, *Hadron Production in Hadron Hadron and Lepton Hadron Collisions*, in 14th Topical Conference on Hadron Collider Physics, eds. M. Erdmann, T. Müller (Springer, Heidelberg, 2003) pp. 161–170 [hep-ph/0211008]
28. W.-K. Tung, S. Kretzer, C. Schmidt, J. Phys. G **28**, 983 (2002) [hep-ph/0110247]
29. B.A. Kniehl, G. Kramer, I. Schienbein, H. Spiesberger, Phys. Rev. D **71**, 014018 (2005) [hep-ph/0410289]
30. G. Kramer, H. Spiesberger, Eur. Phys. J. C **38**, 309 (2004) [hep-ph/0311062]
31. B.A. Kniehl, G. Kramer, I. Schienbein, H. Spiesberger, Eur. Phys. J. C **41**, 199 (2005) [hep-ph/0502194]
32. CTEQ Collaboration, J. Pumplin et al., JHEP **07**, 012 (2002) [hep-ph/0201195]
33. H. Jung, *Unintegrated Parton Density Functions in CCFM*, in XII International Workshop on Deep Inelastic Scattering (DIS 2004), eds. D. Bruncko, J. Ferencei, P. Stríženec, Vol. 1 (SAS, Apr. 2004) pp. 299–302 [hep-ph/0411287]
34. M. Glück, E. Reya, A. Vogt, Phys. Rev. D **46**, 1973 (1992)
35. P. Nason, C. Oleari, Nucl. Phys. B **565**, 245 (2000) [hep-ph/9903541]
36. J. Binnewies, B.A. Kniehl, G. Kramer, Phys. Rev. D **58**, 014014 (1998) [hep-ph/9712482]
37. B.A. Kniehl, G. Kramer, I. Schienbein, H. Spiesberger, Phys. Rev. Lett. **96**, 012001 (2006) [hep-ph/0508129]
38. B.A. Kniehl, G. Kramer, Phys. Rev. D **74**, 037502 (2006) [hep-ph/0607306]
39. L. Gladilin, *Charm Hadron Production Fractions*, 1999, [hep-ex/9912064]
40. T. Sjöstrand et al., Comput. Phys. Commun. **135**, 238 (2001) [hep-ph/0010017]
41. B. Andersson, G. Gustafson, G. Ingelman, T. Sjöstrand, Phys. Rep. **97**, 31 (1983)
42. C. Peterson, D. Schlatter, I. Schmitt, P. Zerwas, Phys. Rev. D **27**, 105 (1983)
43. H. Jung, G.P. Salam, Eur. Phys. J. C **19**, 351 (2001) [hep-ph/0012143]
44. H. Jung, Comput. Phys. Commun. **143**, 100 (2002) [hep-ph/0109102]
45. H. Jung, *The CCFM Monte Carlo Generator CASCADE Version 1.2010*, Nov. 2005, http://www.desy.de/~jung/cascade/
46. M. Ciafaloni, Nucl. Phys. B **296**, 49 (1988)
47. S. Catani, F. Fiorani, G. Marchesini, Phys. Lett. B **234**, 339 (1990)
48. S. Catani, F. Fiorani, G. Marchesini, Nucl. Phys. B **336**, 18 (1990)
49. G. Marchesini, Nucl. Phys. B **445**, 49 (1995) [hep-ph/9412327]
50. S. Frixione, M.L. Mangano, P. Nason, G. Ridolfi, Phys. Lett. B **348**, 633 (1995) [hep-ph/9412348]
51. G. Heinrich, B.A. Kniehl, Phys. Rev. D **70**, 094035 (2004) [hep-ph/0409303]
52. H1 Collaboration, S. Aid et al., Z. Phys. C **69**, 27 (1995) [hep-ex/9509001]
53. R. Brun, F. Bruyant, M. Maire, A.C. McPherson, P. Zanarini, *GEANT 3 User's Guide*, 1987
54. H1 Collaboration, C. Adloff et al., Phys. Lett. B **528**, 199 (2002) [hep-ex/0108039]